Eur. Phys. J. B **41**, 31–42 (2004)
DOI: 10.1140/epjb/e2004-00290-x

THE EUROPEAN PHYSICAL JOURNAL B

Local structure around Ce in the $Nd_{2-x}Ce_xCuO_{4\pm\delta}$ superconductor probed by EXAFS

P. Ghigna[1,a], G. Spinolo[1], E. Santacroce[1], S. Colonna[2], S. Mobilio[3], M. Scavini[4], and R. Bianchi[5]

[1] INSTM, C.S.T.E./CNR, and Dipartimento di Chimica Fisica, Università di Pavia, Viale Taramelli 16, I 27100, Pavia, Italy
[2] CNR Istituto Struttura della Materia, Via Fosso del Cavaliere 100, 00133 Roma, Italy
[3] Istituto Nazionale di Fisica Nucleare & Dipartimento di Fisica, Università di Roma III, Via della Vasca Navale 84, 00146 Roma, Italy
[4] Dipartimento di Chimica Fisica ed Elettrochimica, Università di Milano, via C. Golgi, 19, 20133 Milano, Italy
[5] Istituto CNR di Scienze e Tecnologie Molecolari ISTM, via C. Golgi, 19, 20133 Milano, Italy

Received 30 October 2002 / Received in final form 19 February 2004
Published online 30 September 2004 –

Abstract. The local structure around the Ce substitutional defects has been investigated by Ce and Nd K-edge EXAFS on $Nd_{2-x}Ce_xCuO_{4\pm\delta}$ samples with different dopant concentrations ($x = 0.05$, 0.10, 0.15 and 0.20) and oxygen amounts. The lattice distortion around the $Ce^{\bullet}_{Nd}$ can be described as a shrinkage of the oxygen cuboid along the z crystallographic direction. Moreover, the CuO_4 planes become corrugated. The lattice distortion is well localized and is largely independent of temperature and Ce and oxygen content. EXAFS measurements made at the Nd-K edge indicate that the local chemical environment of Nd is not distorted. The difference electron density maps, obtained from low temperature single crystal X-ray diffraction data, revealed three strong positive residuals which have been ascribed to cerium (at 0, 0, $z \cong 0.41$) and to two non equivalent oxygen apical positions O3 (at 0, 0, $z \cong 0.19$) and O4 (at 0, 0 $z \cong 0.24$). The electron population of O4 site, which is closer to cerium ($d_{Ce-O4} = 1.96$ Å), is 3−4 times the O3 one.

PACS. 61.10.Ht X-ray absorption spectroscopy: EXAFS, NEXAFS, XANES, etc. – 74.72.Jt Other cuprates, including Tl and Hg-based cuprates – 61.72.Ji Point defects (vacancies, interstitials, color centers, etc.) and defect clusters

1 Introduction

The $Ln_{2-x}Ce_xCuO_{4\pm\delta}$ family (Ln = Pr, Nd, Sm, Eu) has attracted much attention as a model system for investigating high-temperature superconductivity. This system, first discovered by Tokura et al. [1,2], shows indeed a number of interesting features. A challenging difference from the large majority of cuprate superconductors is the negative sign of the charge carriers. As a matter of fact, the amount of electrons plays a role similar to that played by the amount of holes in other superconductor families [3–7].

The chemical processes which modify the amount of carriers are: a) cerium doping, and b) interaction with external oxygen leading to inclusion of interstitial oxygen atoms [8].

Each substitutional $Ce^{\bullet}_{Nd}$ defect injects one electron [9]. External oxygen can fill normally empty sites in apical position with respect to Cu [10–14]: fully ionized interstitial oxygens remove two electrons per added oxygen. Superconductivity is achieved in these materials when both doping mechanisms are finely tuned: the cerium content must range between 0.13 and 0.17 and the highest T_C (∼25 K) is given by $x = 0.15$ [15], but the superconducting phase is obtained only with a suitably low oxygen content because interstitial oxygen removes the charge carriers. For a detailed description of the defect structure in this system see [16].

The local order and lattice distortions around the Ce dopants play a central role on the superconductivity of these materials, and have been actively studied in recent years by various groups using different techniques [9,17–21], but a complete study aiming at clarifying these aspects is still lacking. Moreover, there is a growing interest towards local lattice distortions and their effects on amount and mobility of the electronic carriers in the various classes of oxide superconductors [22].

Aim of this work is to study the local atomic structure around the Ce doping atoms and its relationship with oxygen stoichiometry in the $Nd_{2x}Ce_xCuO_{4\pm\delta}$ phase. This goal has been accomplished by Extended X-ray Absorption Fine Structure (EXAFS) measurements at the Nd and Ce K-edges and by X-ray electron density studies at low temperature.

[a] e-mail: paolo.ghigna@unipv.it

2 Experimental

2.1 Synthesis

Powder samples of $Nd_{2-x}Ce_xCuO_{4\pm\delta}$ with $x = 0.05$, 0.10, 0.15 and 0.20 have been prepared by solid state synthesis starting from appropriate mixtures of Nd_2O_3 (Aldrich 99.9%), CeO_2 (Aldrich 99.99%) and CuO (Fluka 99.9%). Details on the synthesis have been reported elsewhere [23,24]. For each cerium content two samples have been prepared with different oxygen contents hereafter named 'oxygen rich' and 'oxygen poor'.

'Oxygen rich' samples were prepared by annealing the as prepared material in pure oxygen flux at 900 °C for 48 h, and slowly cooling down to room temperature, at a rate of 1 °C/h. 'Oxygen poor' samples were prepared by annealing for 96 h the as prepared material at 900 °C under an oxygen-in-nitrogen flux with $P(O_2) = 1.8\times10^{-6}$ atm, and quenching. Only the $x = 0.15$ 'oxygen poor' sample shows superconductivity with $T_C = 25$ K. According to XRPD (X-Ray Powder Diffraction) and EMPA (Electron Micro-Probe Analysis) all the samples are monophasic and homogeneous in the chemical composition.

The $Nd_{1.93}Ce_{0.07}CuO_{4\pm\delta}$ single crystal used for X-ray diffraction analysis has been produced through the "CuO flux method" described in reference [25] and annealed following the same procedure described for the polycrystalline 'oxygen rich' sample. The crystal composition has been checked through EMPA and confirmed by the value of the lattice constants as determined by X-ray diffraction (see below).

2.2 Instruments and methods

The Ce and Nd K-edge EXAFS measurements were performed at the GILDA CRG beam line of the ESRF synchrotron radiation laboratory (Grenoble, France). EXAFS spectra were collected, using a Si(511) double crystal monochromator, in transmission mode. Ion chambers were employed to measure the beam intensity. The samples were mixed with polyethylene in an agate mortar and pressed to pellets. The amount of sample in the pellets was adjusted to ensure an edge jump of about 0.6. Sample pellets were clamped on the cold finger of a liquid He cryostat to control the temperature.

To check the energy stability of the monochromator during the experiment, random duplicate scans have been performed; the scan to scan reproducibility has always been found to be better than 99.9%; in addition the results of the fittings performed on the different duplicate scans were undistinguishable.

The Ce-K edge measurements have been performed on the $x = 0.05$, 0.10, 0.15 and 0.20 samples at 77 K. For the $x = 0.15$ composition, that can give rise to the superconducting phase, the spectra have been collected between 10 K and 280 K. As reference samples Ce and Nd oxides were used.

The EXAFS analysis was performed using the GNXAS code [26,27]. As the GNXAS package does not allow spectral Fourier filtering, the EXCURV98 [28] code was used to analyze the Fourier-filtered EXAFS-difference data described below (Sect. 4). Amplitudes and phase-shifts functions were theoretically calculated by the programs. The coordination distances were assumed to follow Gaussian distributions, and, therefore, only the Gaussian part of the Debye-Waller factor (σ^2) was modelled. Random tests were performed in order to check for the presence of higher order cumulants in the distance distributions, always with negative results. For both the Ce and Nd-K edge spectra, the number of independent points is always greater than 30 and, therefore, well above the number of parameters used in the fits (respectively 15 and 22 for the Ce and Nd spectra). Due to the high correlations between the fitting parameters, the errors calculated by the programs were always under-estimated. Therefore, we used an arbitrary procedure which consisted in manually varying each parameter, all the other parameters held fixed. Whenever a detectable difference was found between the experimental and the calculated EXAFS Fourier transforms, we assumed the difference between this value and the fitted parameter as the error. In this case we always obtained an error greater than that obtained by the programs. With this procedure, the errors could be over-estimated, but we think that this is safer than having under-estimated error bars.

Table 1. Crystal data.

Formula	$Nd_{2-x}Ce_xCuO_{4\pm\delta}$
Colour	Black
Habit	Disk
Dimensions	$60 \times 55 \times 25$ μm^3
Space group	I4/mmm
Z value	2
μ (MoKα)	32.8 mm^{-1}
Temperature	90 K
Radiation	0.71073 (MoK$_\alpha$)
Scan type	$\omega - \varphi$
Max. 2θ.	119.28°
Sphere of data	$-9 \le h \le 9$
	$-9 \le k \le 9$
	$-29 \le l \le 28$
Total n. of Reflections	9974
n. of unique Reflections	464
Cell parameter a(Å)	3.9353(2)
Cell parameter c(Å)	12.0874(9)

For the X-ray diffraction (XRD) measurements the disk shaped single crystal ($60 \times 55 \times 25$ μm^3) has been mounted on a Bruker SMART CCD area-detector diffractometer (graphite-monochromatised Mo K_α radiation, $\lambda = 0.71073$ Å). Data were collected at 90 K, following a multi-scan strategy. Table 1 summarizes the experimental details.

For cell refinement, data reduction and multiscan absorption correction the *SAINT* and *SADABS* by Bruker

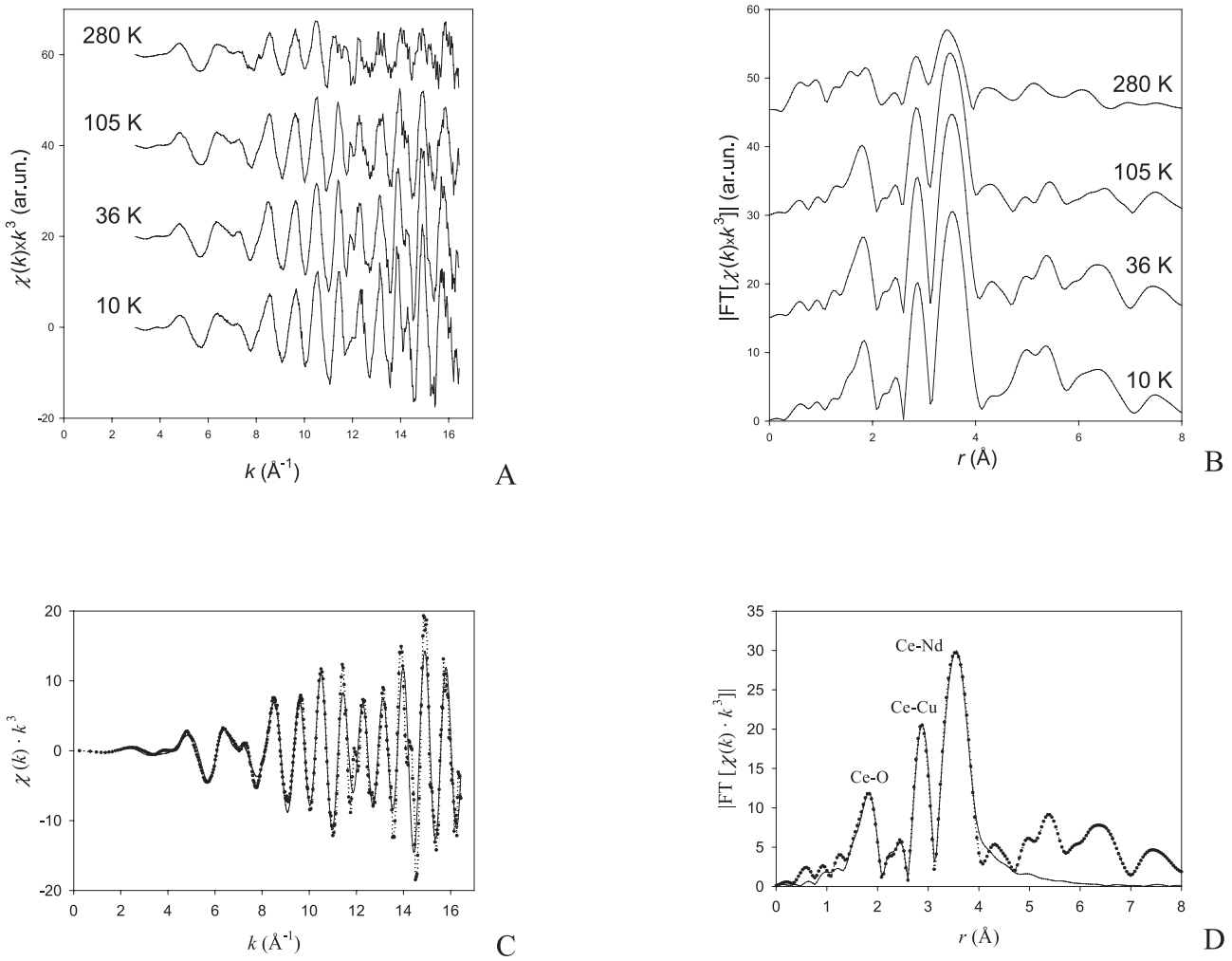

Fig. 1. A: Ce-K edge EXAFS signals for the 'oxygen poor' sample at selected temperatures. B: the corresponding Fourier transforms. C: fitting of the EXAFS spectrum at 36 K. D: the corresponding Fourier transform. In these last two panels, dots and dotted lines correspond to the experimental, the full line to the fit according to the structural model of Figure 2.

programs have been utilised [29]. Structure solution (direct methods) and preliminary structure refinements were performed by means of *SHELX97* program [30].

The final refinements of scale factor, extinction, positional, temperature and occupation parameters were carried out with the VALRAY system implemented by Stewart and Spackman [31]. This code enables the derivation of an exhaustive set of electrostatic properties using a flexible, nucleus centred, pseudoatom multipole expansion of the electron density in crystals starting from an accurate set of X-ray diffraction data.

Nd^{3+}, Ce^{4+}, Cu^{2+} and O^{-} scattering factors and Anomalous Scattering factors were taken from *International Tables for Crystallography* [32].

3 Results

3.1 Ce-K edge EXAFS measurements

Ce-K edge EXAFS signals at various temperatures for the superconducting sample are shown in Figure 1A. Strong EXAFS oscillations, well above the noise level, are observed up to 16 $Å^{-1}$. The statistical noise in the $\chi(k)$ was estimated by fitting a straight line on the high energy tail of the absorption spectra, where the EXAFS oscillations are undetectable, i.e. above 41 700 eV, roughly corresponding to $k = 20$ $Å^{-1}$. The noise is, therefore, estimated from the standard deviation of the residual signal which is of the order of 10^{-3} after normalisation by the edge jump. Figure 1B shows the Fourier transforms of the EXAFS oscillations reported in Figure 1A.

According to the crystal structure reported in Figure 2 and using the model cluster shown in the inset of the same figure, we calculated a theoretical EXAFS signal to fit the experimental one. The model cluster used in the data analysis takes into account coordination shells around Ce up to a radial distance of 4 Å. This corresponds to six coordination shells around the absorbing cerium: here denoted as Ce-O1, Ce-O2, Ce-Cu, Ce-Nd1, Ce-Nd2, and Ce-Nd3 in order of increasing distance. In the reference structure (Nd_2CuO_4), all Nd sites are symmetry related, whereas there are two oxygen sites: here, Nd1, Nd2 and Nd3

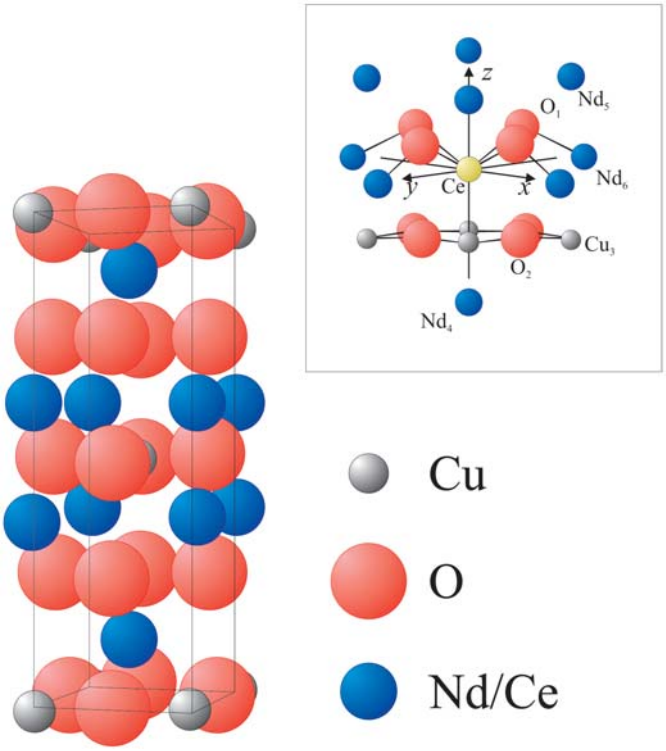

Fig. 2. Nd_2CuO_4 crystal structure. In the inset, the model cluster used for the EXAFS simulations. The distances between the central cerium ion and its neighbours are calculated from the spectrum of Figure 1.

denote three crystallographically equivalent Nd sites, which are at different distances from a specific Nd site occupied by the Ce dopant; O1 and O2 denote oxygen atoms which are at different distances from Ce defects and are also in crystallographically non-equivalent sites [1].

Actually, the EXAFS Fourier transform (Fig. 1) shows further components well above 4 Å, but their interpretation would be obviously much less accurate. This paper mainly focuses on lattice distortions close to the dopants and we preferred to use the minimum amount of parameters necessary to extract the needed information. Therefore, the Fourier components above 4 Å have not been analysed in the whole set of spectra. In the fitting procedure the bond lengths (R), and the Debye-Waller factors (σ^2) were used as free parameters.

In Figures 1C and D an example of the fit quality is given for $T = 36$ K. In the two figures the dots represent the experimental signal and the full line the result of the fit. The numerical results, representative of the fit quality for all spectra, are reported in Table 2.

In the EXAFS Fourier transform, the first two oxygen coordination shells originate an unresolved peak at ∼1.8 Å (marked as Ce-O on Fig. 1D), the copper shell gives rise to a peak at ∼2.9 Å (marked as Ce-Cu). The main peak at ∼3.5 Å is the overlap of the three different Ce-Nd shells (marked as Ce-Nd).

Although the fitted Ce-Nd distances are in good agreement with crystallographic data (see Tab. 2), the correlations between them due to this overlap are too large to make the fitted Ce-Nd distances sufficiently reliable. Therefore, the following analysis will focus on the parameters related to the first three shells. A significant correlation was also found between the parameters of the Ce-O1 and Ce-O2 shells due to the strong overlap of the two peaks.

Table 2. EXAFS fitting parameters for the spectrum of Figure 1. r: distances; σ^2: distance variances; for comparison, the distances calculated from the pertinent lattice constants are reported as r_0.

Shell	Atom	r(Å)	σ^2 (Å^2)	r_0 (Å)
1	O1	2.21(1)	0.0033(1)	2.32
2	O2	2.63(1)	0.007(1)	2.67
3	Cu	3.33(1)	0.0019(1)	3.32
4	Nd1	3.55(1)	0.0044(1)	3.60
5	Nd2	3.72(1)	0.0031(1)	3.71
6	Nd3	3.96(1)	0.0015(1)	3.95

The Ce-O1, Ce-O2 and Ce-Cu distances in $Nd_{2-x}Ce_xCuO_{4\pm\delta}$ are shown in Figure 3 as a function of temperature, for the $x = 0.15$ sample in both 'oxygen poor' and 'oxygen rich' forms. Clearly, within the experimental error, the coordination distances are independent of T. The Ce-O1, Ce-O2 and Ce-Cu distances in $Nd_{2-x}Ce_xCuO_{4\pm\delta}$ samples with different cerium content (x) are displayed in Figure 4. Actually, the temperatures of the experiments are 77 K for the $x = 0.05$, 0.10 and 0.20 samples, and 61 K for the $x = 0.15$ samples, but the results can safely be compared in light of what has been shown in the previous figures. Within the experimental error, the results show that the Ce-O1, Ce-O2 and Ce-Cu distances are also independent of x. Most important here is their comparison with the Nd-O1, Nd-O2 and Nd-Cu distances, calculated from the pertinent lattice constants [33], which are shown in the same figures as straight lines. The Ce-O1 and Ce-O2 distances are much smaller than the corresponding Nd-O1 and Nd-O2 distances, while the Ce-Cu and Nd-Cu distances are not significantly different. Also, the Ce-O1 coordination distance, which is the shortest one, undergoes the strongest modification with respect to the reference Nd-O1 bonding distance.

In Figure 5 the temperature dependence of the Debye-Waller factors (σ^2) measured at the Ce K-edge for the $x = 0.15$ sample are shown. The σ^2 factors show the expected trend with temperature: they are almost independent of temperature up to ∼60 K, then they increase with T.

The Debye-Waller factor is composed of two square summed terms [34]:

$$\sigma^2 = \sigma_S^2 + \sigma_d^2(T)\,. \tag{1}$$

The dynamic term ($\sigma_d^2(T)$) is related to the thermal vibrations, thus, its amplitude is temperature dependent and decreases decreasing temperature. The static term (σ_S^2) is independent of temperature and proportional to the disorder around the absorbing site. To fit $\sigma_d^2(T)$ we used

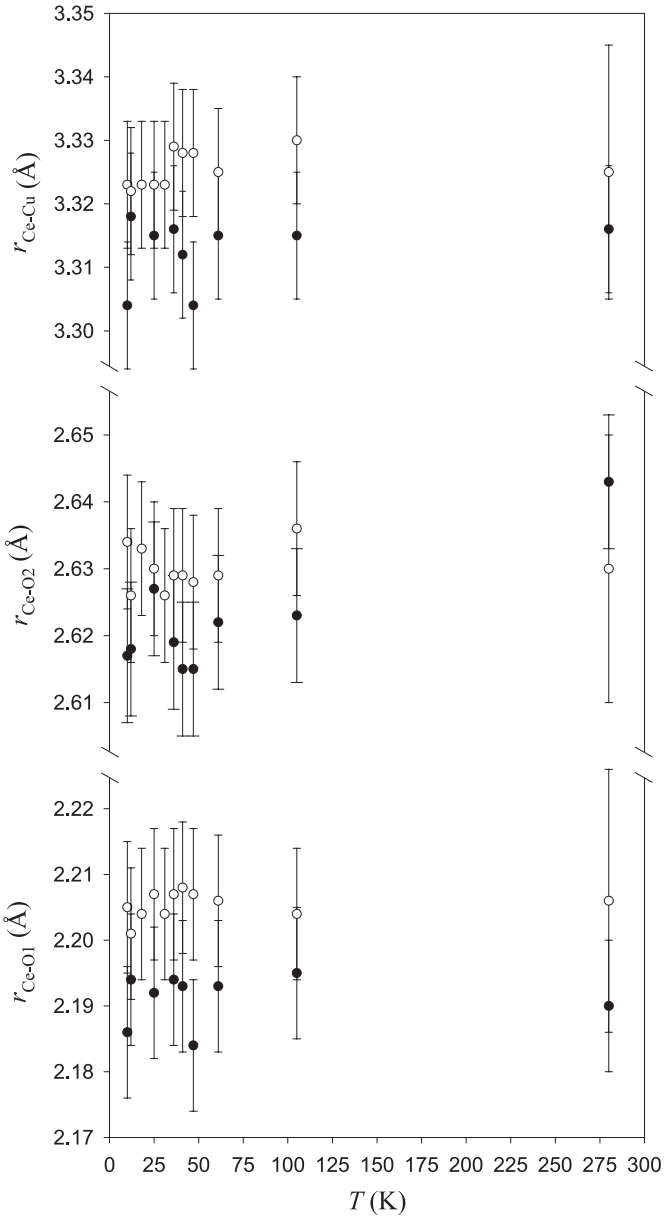

Fig. 3. Ce-O1, Ce-O2 and Ce-Cu distances measured on the $x = 0.15$ samples as a function of T. Hollow symbols: 'oxygen poor' phase; full symbols: 'oxygen rich' phase.

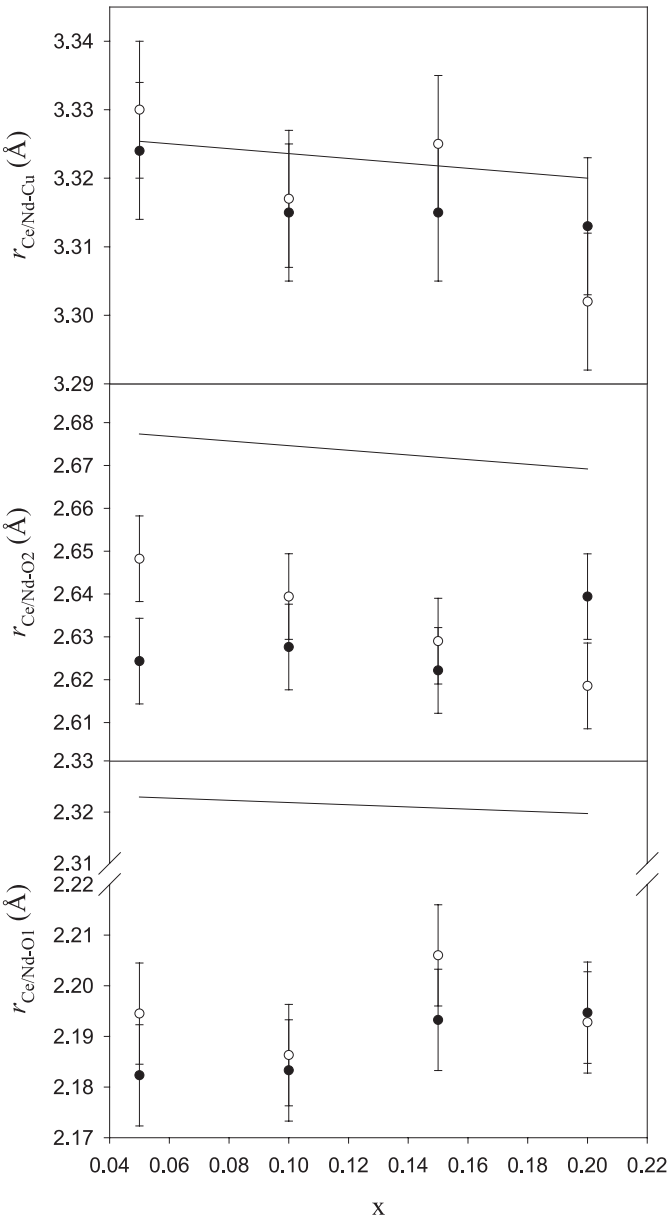

Fig. 4. Distance Ce-O1 (lower panel), Ce-O2 (middle panel) and Ce-Cu (upper panel) as a function of x. Hollow symbols: 'oxygen poor' sample, as obtained from EXAFS; full symbols: 'oxygen rich' sample, as obtained from EXAFS; full lines: Ce/Nd-O1, Ce/Nd-O1 and Ce/Nd-Cu, calculated from the pertinent lattice constants as explained in the text.

the Einstein correlated model which considers the pair of absorber and backscatterer atoms as an independent oscillator with frequency ω_E [35]. The σ^2 values as a function of temperature were fitted using this model giving as a result an Einstein temperature $\Theta_E = \hbar\omega_E/k_B$ (k_B is the Boltzman constant) and σ_S^2 proportional to the disorder around the dopant atoms. Table 3 gives the results of such a fitting procedure. As can be seen from Table 3 we found negative values for some static terms of the Debye-Waller factors. This behaviour can be explained by considering that in the σ^2 results of the EXAFS fitting procedure there might be systematic errors giving rise to a displacement of the scale reference. Thus, these values cannot be used in an absolute way but only in the comparison to the Nd measurements (see next paragraph). Inspecting the temperature dependence of the σ^2 values it is interesting to look for any anomalous behaviour at T_c. In Figure 5 the result of the fit is represented by a continuous line. We did not find any anomaly at the transition temperature of the σ^2 factors in contrast to other works appeared in literature concerning other high T_c superconducting systems (see for example Ref. [36]).

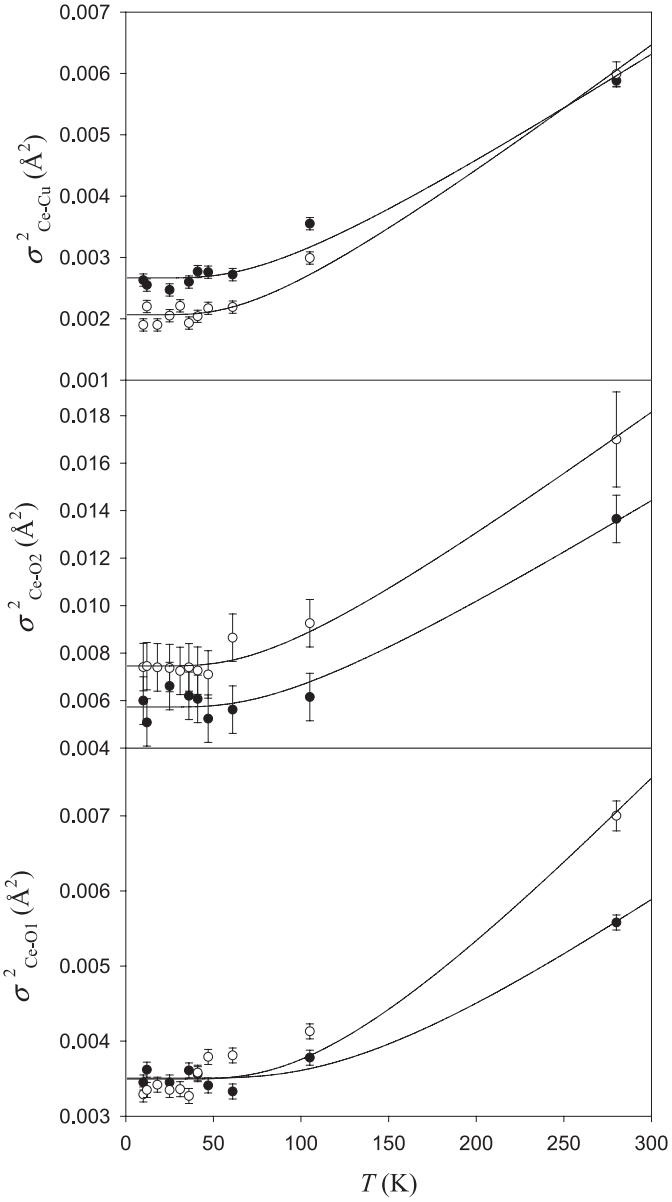

Fig. 5. Debye-Waller factors (σ^2) of the Ce-O1, Ce-O2 and Ce-Cu distance as a function of T for the $x = 0.15$ sample. Hollow symbols: 'oxygen poor' sample; full symbols: 'oxygen rich' sample.

3.2 Nd-K edge EXAFS measurements

Figure 6A shows the Nd-K edge EXAFS oscillations at various temperatures for the $x = 0.15$ 'oxygen poor' sample; the corresponding Fourier transforms are shown in Figure 6B. Comparing Nd-K edge data to the Ce ones of Figure 1 two differences are apparent: a) the EXAFS oscillations are clearly seen above the noise level up to 20 Å^{-1} and b) the presence of quite intense peaks in the Fourier transform at $r \geq 5$ Å. These peaks are attributed to Nd-O2-Nd and Nd-Cu-Nd multiple scattering paths. Since the Nd-O2-Nd and Nd-Cu-Nd angles are equal to 180° these multiple scattering contributions are expected to be quite intense. The much lower intensity of the multiple scattering peaks in Ce-K edge spectra is the evidence of a considerable amount of static disorder around the $Ce^{\bullet}_{Nd}$ defects. Generally speaking, several effects can modulate the EXAFS amplitude; but *in this case* we are comparing the local order of different cations in the *same* site of the *same* (ordered) structure. Consequently, the reduction of the multiple scattering amplitude signals may only be ascribed to the presence of disorder around the Ce doping atoms. Therefore, the Nd-K edge spectra were fitted using the same model as described before for the Ce-K edge EXAFS spectra, adding Nd-O2-Nd and Nd-Cu-Nd multiple scattering paths with effective scattering lengths of 5.36 Å and 6.66 Å, respectively. In Figure 6C the EXAFS signal is shown for $T = 40$ K (dots) compared to the fitting curve (continuous line) to give a reference of the fit quality for the Nd-K edge measurements. Figure 6D shows the Fourier transforms of the experimental signal and the fit. The parameters obtained by the fit are affected by the same systematic errors and correlations as described before for the Ce-K edge data.

In Figure 7 the Nd-Cu, Nd-O2 and Nd-O1 distances, respectively, are reported as a function of temperature for all the samples. In the same figure, the full lines refer to the crystallographic distances in pure Nd_2CuO_4 (neglecting the dependence on T). It is easily noted that all the distances in all the samples impressively agree with the crystallographic ones. This is a nice confirmation of the quite localized nature of the lattice distortions around the $Ce^{\bullet}_{Nd}$ defects. Moreover, we do not find evidence of structural changes at any temperature.

The σ^2 parameters for Nd-O1, Nd-O2 and Nd-Cu coordination shells as a function of temperature are displayed in Figure 8. These values were fitted, as in the Ce case, using the model described in equation (1). The resulting Einstein temperatures and static terms are reported in Table 3.

The data in Table 3 show no strong differences in Θ_E values, with respect to the Ce and Nd sites and oxygen content, except for the Ce-O1 coordination shell where the presence of extra oxygen strongly increases the Einstein temperature value. The amount of static disorder is similar in each coordination shell for all the samples, and it is considerably smaller than that displayed in the Ce-K edge data. Again, this is in agreement with the quite localised nature of the lattice distortions around the $Ce^{\bullet}_{Nd}$ defects.

3.3 X-ray diffraction

A preliminary cell has been determined at room temperature (291 K) in order to establish the cerium concentration in the structure. The cell constant values equal to $a = 3.9456(4)$ Å and $c = 12.126(2)$ Å are consistent with $x = 0.07$ nominal composition, according to Paulus et al. [37]. Lowering the temperature down to 90 K, the cell constants became $a = 3.9353(2)$ Å and $c = 12.0874(9)$ Å.

A first refinement on the low temperature XRD data has been performed with a "pure" structural model; only the four non equivalent atomic positions of the ideal

Table 3. Einstein temperatures for $x = 0.15$ samples determined by the fitting of the Debye-Waller factors as a function of the temperature.

Ce K-edge

	Ce-O1		Ce-O2		Ce-Cu	
	Θ_E (K)	σ_S^2 (Å^2)	Θ_E (K)	σ_S^2 (Å^2)	Θ_E (K)	σ_S^2 (Å^2)
$x = 0.15$ oxygen rich	433 ± 15	−0.00034(17)	267 ± 3	−0.00053(12)	242 ± 6	0.00040(11)
$x = 0.15$ oxygen poor	371 ± 8	−0.00076(14)	246 ± 2	0.00066(12)	224 ± 5	−0.00038(10)

Nd K-edge

	Nd-O1		Nd-O2		Nd-Cu	
	Θ_E (K)	σ_S^2 (Å^2)	Θ_E (K)	σ_S^2 (Å^2)	Θ_E (K)	σ_S^2 (Å^2)
$x = 0.15$ oxygen rich	380 ± 16	−0.00104(23)	223 ± 6	−0.00459(27)	189 ± 9	−0.00118(24)
$x = 0.15$ oxygen poor	401 ± 20	−0.00113(24)	257 ± 9	−0.00279(30)	188 ± 9	−0.00146(25)

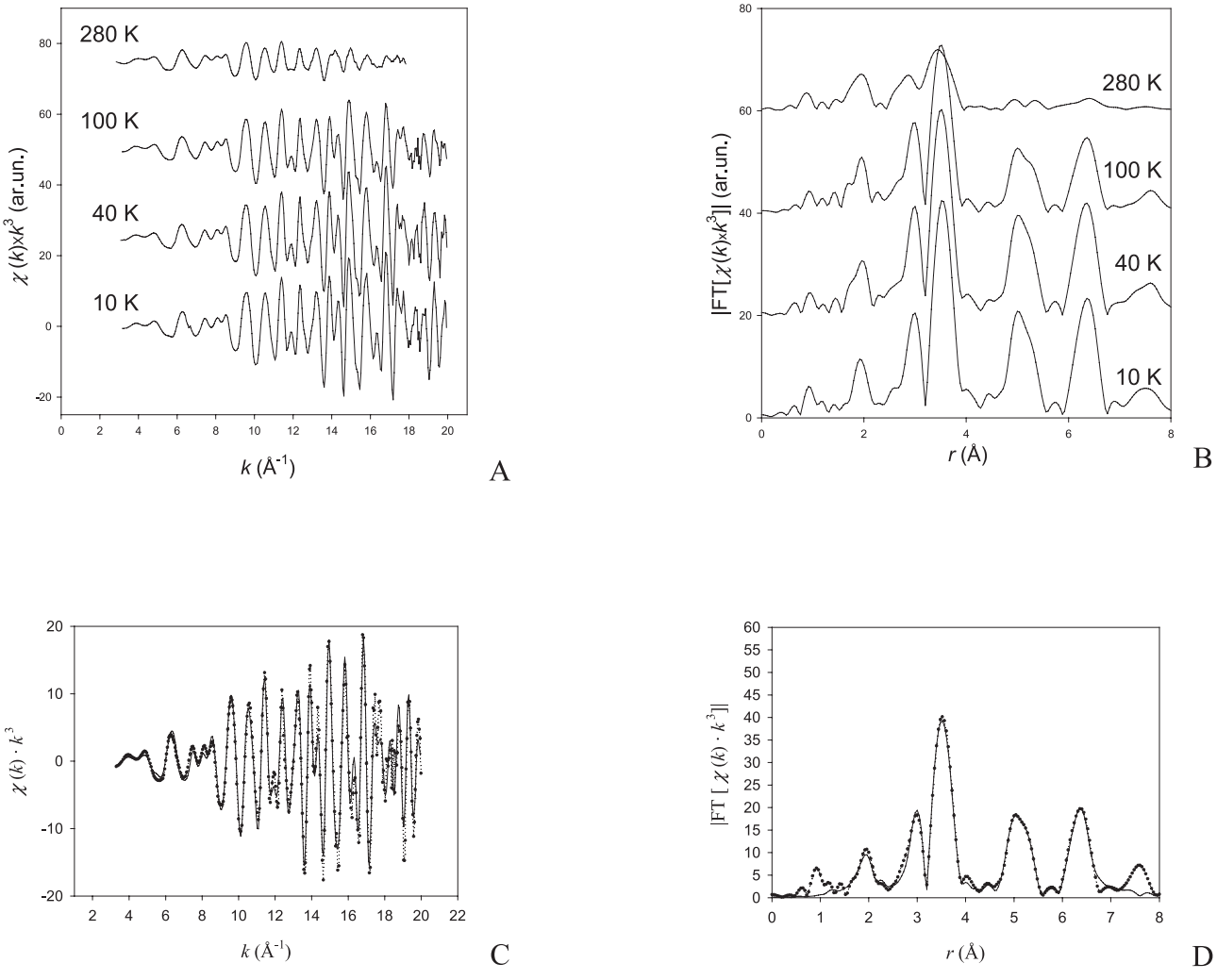

Fig. 6. A: Nd-K edge EXAFS signals for the 'oxygen poor' sample at selected temperatures. B: the corresponding Fourier transforms. C: fitting of the EXAFS spectrum at 40 K. D: the corresponding Fourier transform. In these last two panels, dots and dotted lines correspond to the experimental, the full line to the fit obtained as indicated in the text. Multiple scattering contributions are clearly apparent at high r ($\geq$5 Å).

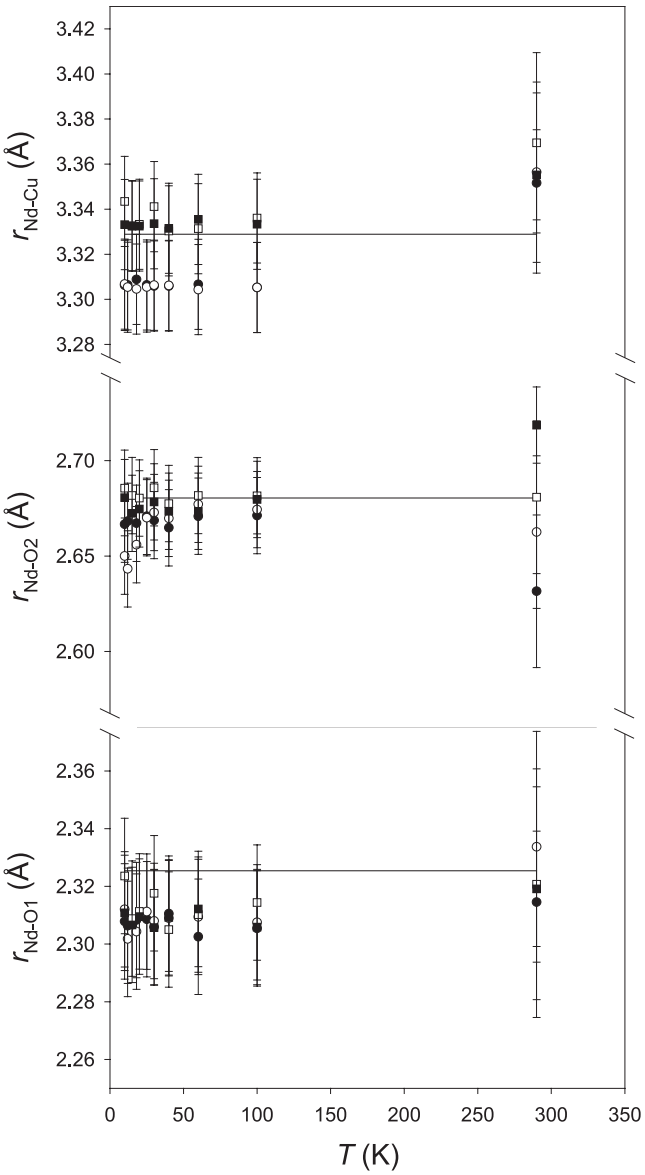

Fig. 7. Nd-O1, Nd-O2 and Nd-Cu distances as a function of T. Hollow symbols: 'oxygen poor' samples; full symbols: 'oxygen rich' samples; circles: $x = 0$ samples; squares: $x = 0.15$ samples. The continuous line give the distances obtained from the crystallographic data.

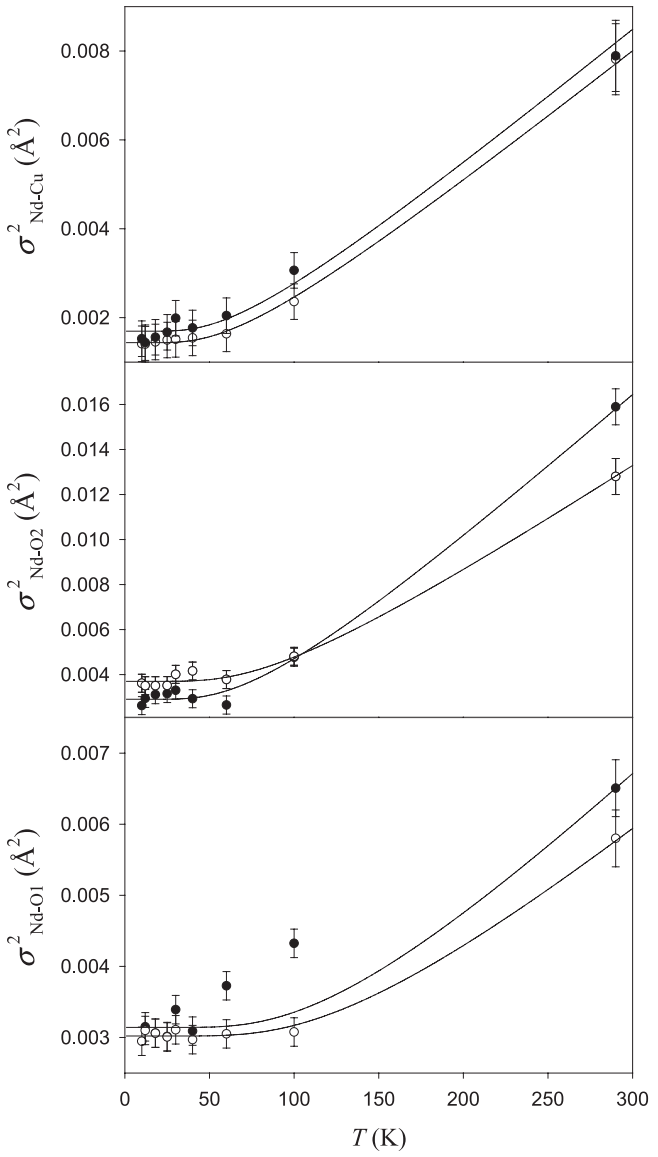

Fig. 8. Debye-Waller factors (σ^2) of the Nd-O1, Nd-O2 and Nd-Cu distance as a function of T for the $x = 0.15$ sample. Hollow symbols: 'oxygen poor' sample; full symbols: 'oxygen rich' sample.

Nd_2CuO_4 structure, i.e. Nd1 at (0, 0, z); Cu1 at (0, 0, 0); O1 at (0, $^1/_2$, $^1/_4$) and O2 at (0, $^1/_2$, 0) have been used. Within this model the electron populations have been fixed to full site occupation, while z(Nd1), anisotropic temperature factors and a secondary extinction coefficient have been allowed to vary.

Table 4 summarises the result of the refinement. We can note that all the thermal ellipsoids are elongated in the c-direction (see Tab. 4). A similar anisotropy can be observed even in cerium free $Nd_2CuO_{4\pm\delta}$ samples [12,38,39]. As a consequence we can infer that it is mainly due to the difference in the bond strength along the three axis. For example copper is in a square planar coordination with the four next neighbours oxygen ions lying in the ab plane (see Fig. 2), and we expect the observed greater vibration amplitude along the c-direction. The above discussed distortion induced by cerium doping is expected to have little effect on the anisotropic thermal parameters as it involves only a few percent of ions in agreement with the local nature of the distortion.

Figure 9 reports the Fourier Difference Density (FDD) map relative to the $ac\,(b = 0)$ plane. For the FDD map, reflections up to $\sin\theta/\lambda = 1.05$ Å^{-1} have been used, in order to emphasise the contribution of core electrons (static and dynamic disorder) with respect to valence (bonding) electrons. In Figure 9 three sharp FDD peaks are apparent along the c axis, namely at (0, 0, ∼0.19), (0, 0, ∼0.24) and (0, 0, ∼0.41) positions.

Table 4. Atomic fractional coordinates, anisotropic temperature factors (Å^2), site multiplicity (positions per cell) and electron populations (electrons per atom) for the "pure model". The anisotropic temperature factor is defined by $\exp\{-8\pi^2[(ha^*/2)^2U_{11}+(kb^*/2)^2U_{22}+(lc^*/2)^2U_{33}]\}$.

Atom	x/a	y/b	z/c	U_{11} (Å^2) $\times 10^4$	U_{22} (Å^2) $\times 10^4$	U_{33} (Å^2) $\times 10^4$	Electron population	Site multiplicity
Nd1	0	0	0.35187(2)	15.3(3)	$\equiv U_{11}$	18.3(5)	57	4
Cu1	0	0	0	19(1)	$\equiv U_{11}$	30(2)	27	2
O1	0	0.5	0.25	43(5)	$\equiv U_{11}$	52(8)	10	4
O2	0	0.5	0	57(9)	36(8)	67(8)	10	4

$R(F) = \Sigma||F_o| - k|F_c||/\Sigma|F_o| = 0.0237$
$wR(F^2) = [\Sigma w(||F_o|^2 - k^2|F_c|)^2/\Sigma w|F_o|^4]^{1/2} = 0.0514$
$GoF = [\Sigma w(||F_o|^2 - k^2|F_c|)^2/(N_0 - N_p]^{1/2} = 2.8621$
where F_o and F_c are the observed and calculated structure factors, $w = 1/\sigma^2(F_0)$, k is the scale factor, N_0 is the number of independent observations and N_p is the number of the fitting parameters.

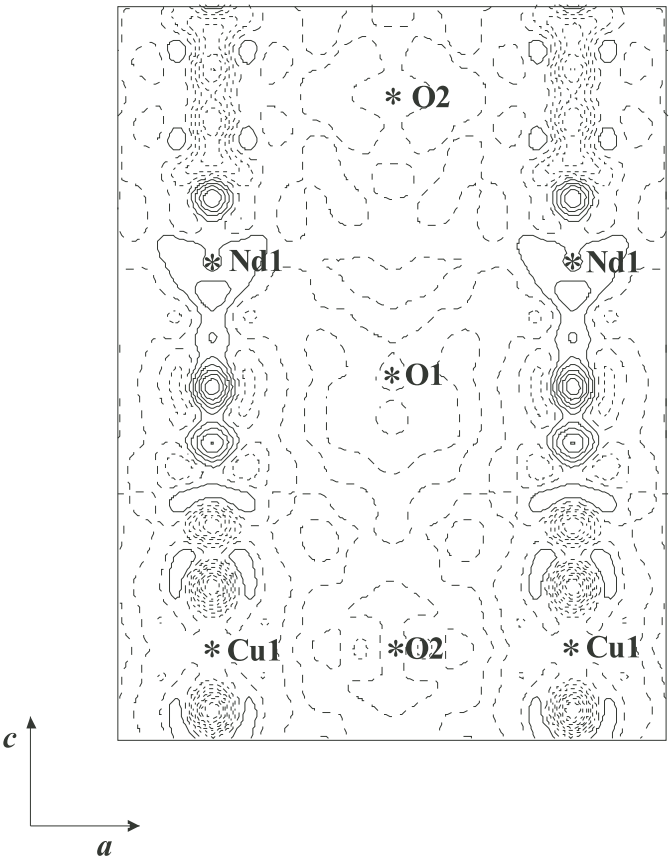

Fig. 9. Fourier difference density map on the ac (b=0) plane pertinent to the "pure" model. Asterisks mark the ion positions. Contour intervals at 1 e Å^{-3}. Solid lines represent positive contour, short dashed lines represent negative contour and the wide dashed line represents zero contour.

Concerning the first two peaks (at $z \cong 0.19$ and $z \cong 0.24$), their positions are close to the one of the apical oxygen claimed by several authors [11–13,40]. It is worth noting that Schultz et al. [13] found two peaks at the same positions in FDD maps obtained by neutron diffraction performed at 15 K on oxidised $Nd_{1.85}Ce_{0.15}CuO_y$ single crystals. As neutron diffraction is sensitive to nuclear positions this finding clearly points out that these two peaks are not due to electron deformation density.

A first attempt has been made in order to refine alternatively only one of the two positions close to that of the "apical oxygen", but the results obtained were unsatisfactory. Successively, both positions have been refined simultaneously allowing z and electron population to vary and fixing the U_{ij} to those of the O1 site. We tentatively attribute these peaks to two different interstitial oxygen positions and, in the following, they will be named O3 (at $z \cong 0.19$) and O4 (at $z \cong 0.24$) sites. On the O4 site the electron population is 3−4 times the O3 one.

For what concerns the third maximum (at $z \cong 0.41$) we infer that it has to be ascribed to core electron density as its intensity increases with increasing the $\sin\theta/\lambda$ upper limit. Unfortunately, it is not possible to make a comparison with the cited article of Schultz et al. [13] as their maps are truncated at lower z levels. Bram et al. [41] show similar features in their FDD maps derived from XRD measurements performed on a crystal with $x = 0.13$, for $T < 150$ K and claimed a disorder of Nd/Ce position. We tentatively assign the FDD peak at $z \cong 0.41$ to the doping Ce ions.

Table 5 summarises the result of a refinement on a "doped" model; where, in addition to the Nd1, Cu1, O1 and O2 sites, the O3, O4 and Ce1 sites have been introduced. Within this structural model the O3 and O4 anisotropic temperature factors have been fixed equal to that of O1 whereas Ce1 anisotropic temperature factors have been fixed equal to that of Nd1. Electronic populations, positional parameters and secondary extinction coefficient have been allowed to vary. A charge depletion on the Nd1 site is apparent, and, at a minor extent on Cu1 and O1 sites.

The significant improvement of statistical parameters is evident. In Figure 10 the FDD map relative to the same plane and this second model is shown up to $\sin\theta/\lambda = 1.05$ Å^{-1}.

It is worth noting that both O3 and O4 have too short contacts with O1 ions (2.1, 2.0 Å respectively). It is necessary to suppose the presence of local distortion for the O1 ions close to interstitial oxygen position. Moreover, it is not possible to determine from the above data any

Table 5. Atomic fractional coordinates, isotropic temperature (Å^2), site multiplicity (positions per cell) and electron populations (electrons per atom) for the "doped model". The anisotropic temperature factor is defined by $\exp\{-8\pi^2[(ha^*/2)^2U_{11} + (kb^*/2)^2U_{22} + (lc^*/2)^2U_{33}]\}$.

Atom	x/a	y/b	z/c	U_{11} (Å^2) $\times 10^4$	U_{22} (Å^2) $\times 10^4$	U_{33} (Å^2) $\times 10^4$	Electron population	Site multiplicity
Nd1	0	0	0.35186(2)	15.3(3)	$\equiv U_{11}$	18.3(5)	55.9(1)	4
Ce1	0	0	0.4063(4)	≡Nd1	≡Nd1	≡Nd1	0.55(6)	4
Cu1	0	0	0	19(1)	$\equiv U_{11}$	30(2)	26.2(1)	2
O1	0	0.5	0.25	43(5)	$\equiv U_{11}$	52(8)	9.7(1)	4
O2	0	0.5	0	57(9)	36(8)	67(8)	10.0(1)	4
O3	0	0	0.19(1)	≡O1	≡O1	≡O1	0.2(1)	4
O4	0	0	0.244(4)	≡O1	≡O1	≡O1	0.7(1)	4

$R(F) = \Sigma||F_o| - k|F_c||/\Sigma|F_o| = 0.0167$
$wR(F^2) = [\Sigma w(||F_o|^2 - k^2|F_c|)^2/\Sigma w|^{1/2} = 0.02507$
$GoF = [\Sigma w(||F_o|^2 - k^2|F_c|)^2/(N_0 - N_p]^{1/2} = 1.7897$
where F_o and F_c are the observed and calculated structure factors, $w = 1/\sigma^2(F_0)$, k is the scale factor, N_0 is the number of independent observations and N_p is the number of the fitting parameter.

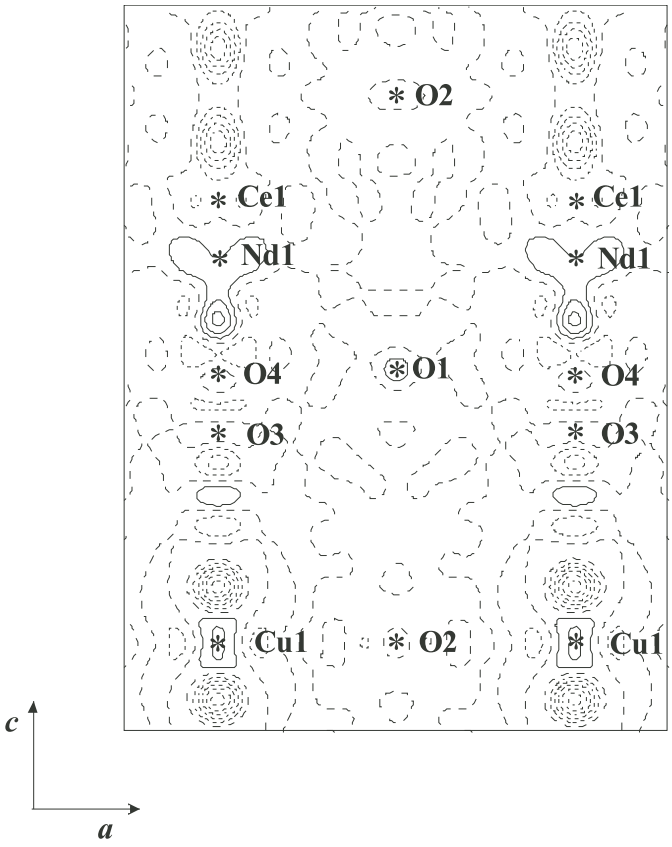

Fig. 10. Fourier difference density maps on the $ac(b = 0)$ plane pertinent to the "doped" model. Asterisks evidence ion positions. Contour as in Figure 8.

preference of O3 and O4 oxygen interstitial ions for Ce or Nd as nearest neighbours, because X-ray diffraction is a probe for the mean structure. On the contrary, EXAFS is sensitive to the local structure and some further information about the defect structure will be shown and discussed in the following section.

4 Discussion

EXAFS measurements have pointed out that the Ce-O distances are significantly smaller than the corresponding Nd-O ones. This corresponds to a collapse of the oxygen coordination cuboid when Ce replaces Nd. Assuming that the distortion is strictly localised around the $Ce^{\bullet}_{Nd}$ defects, the effect on the average cell parameters should have a linear relationship with the doping amount (a form of Vegard's law). This assumption can be tested by comparing the cell dimension along the c-direction as determined by EXAFS, which probes the local structure around Ce defects, and by X-ray diffraction, which probes an average structure. The c parameter can be evaluated as $4 \times [z(\mathrm{O1}) + z(\mathrm{Cu})]$. Since the crystallographic a parameter is well known from diffraction measurements and is almost independent of doping [33], z(O1) and z(Cu) in the cell containing the Ce dopant are easily computed from the Ce-O1 and Ce-Cu distances measured by EXAFS. Then, the corresponding c mean value at composition x is given by the linear combination of EXAFS determined and dopant free ($c_{x=0}$, [33]) lattice constant [9]:

$$c_x = \frac{2-x}{2} c_{x=0} + \frac{x}{2} 4 \left[|z(\mathrm{O1})| + |z(\mathrm{Cu})| \right]. \qquad (2)$$

As both the Ce-O1 and Ce-Cu distances are roughly constant with respect to both x and oxygen content of the sample, a mean value has been used for these quantities. These c_x are then compared with the corresponding quantities given by the X-ray diffraction [33]. The reasonable agreement (see Fig. 11) provides an indirect assessment of the distortion localisation around the $Ce^{\bullet}_{Nd}$ defects, mainly consisting of a shortening along the c crystallographic axis of the Ce-O cuboid. Our findings are in agreement with static lattice energy calculations which predict that the largest effect around the $Ce^{\bullet}_{Nd}$ defects is an atomic relaxation along the z-direction [18]. As a consequence of the oxygen coordination shrinkage around the dopant site, the CuO_4 squares close to the $Ce^{\bullet}_{Nd}$ defects lose their planar geometry and become corrugated. In fact, the Ce-O1

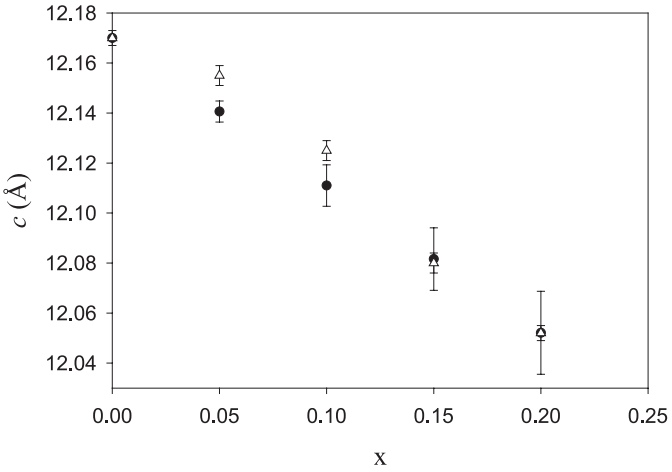

Fig. 11. Lattice constant c as a function of x. Hollow triangles: experimental values from X-ray powder diffraction; full circles: calculated from equation (2) and the EXAFS results.

and Ce-O2 distances are shorter than the corresponding Nd-O1, Nd-O2 distances, whereas the Ce-Cu distance is not significantly different from the Nd-Cu one. This finding is in agreement with previous Cu-K edge EXAFS determinations of the angular distributions for the in plane quasi-linear Cu-O-Cu configuration [42], and with neutron diffraction determinations of the pair distribution functions [17,18].

A close investigation of the Debye-Waller values from the EXAFS analysis will supply a deeper understanding of the dopant effect on the crystal structure. From Table 3 one can note that there exists a sizable difference in σ_S^2 between Ce and Nd sites which demonstrates a greater disorder around Ce sites, as expected. In fact, the majority of Nd atoms see a regular crystal structure with a low static disorder. In the neighbourhood of the Ce sites, on the other hand, the distortion of the crystal lattice gives rise to a spread of the bonding distances which is reflected in a larger static contribution to the Debye-Waller factor. The amount of Ce atoms is small in the structure compared to the Nd atoms, thus the static disorder seen around Nd atoms is almost unmodified by the presence of Ce atoms in the crystal structure. These observations support the localised nature of the distortion around the $Ce^{\bullet}_{Nd}$ defects regardless of the oxygen amount in the sample. The Θ_E values reported in Table 3 indicate that the dynamical properties of the coordination shells around Nd sites are little affected by the oxygen stoichiometry. The same statement applies to the Ce-O2 and Ce-Cu distances. On the other hand, the Ce-O1 coordination shows a sizable Θ_E variation when the oxygen stoichiometry is varied. This can be nicely related to the presence of oxygen interstitials in apical position with respect to copper. In fact, X-ray diffraction measurements detected the presence of apical oxygen atoms in two non equivalent positions, O3 and O4. In particular:

a) the Ce1-O4 distance is 1.96 Å.
b) the Cu-O3 distance is 2.30 Å, in agreement with previous EXAFS determinations [10].
c) the O4 population is 3-4 times the O3 one.

The structural model used for the EXAFS analysis does not contain extra oxygen atoms in interstitial position. This approach is justified by the very small contribution of oxygen atoms in extra positions and results in small systematic errors in the σ^2 factors of the Ce-O shells in oxygen rich samples. The attempt to introduce interstitial oxygen atoms in the cluster model resulted in a small improvement of the fit quality in the 'oxygen rich' samples. But, due to the low intensity of the signal of the interstitial oxygens and the short bonding distance, the sensitivity of this approach is rather poor.

5 Conclusions

The atomic structure around the doping Ce atoms has been studied in the $Nd_{2-x}Ce_xCuO_{4\pm\delta}$. Ce enters the Nd_2CuO_4 structure as $Ce^{\bullet}_{Nd}$. The substitutional defect is associated with a lattice distortion: the oxygen cuboid around each dopant is mainly shrunk along the z crystallographic direction and the CuO_4 planes become corrugated. The lattice distortion is well localised around Ce defects resulting largely independent of temperature as well as of Ce and oxygen content.

Interstitial oxygen atoms have been found in two non equivalent sites, next to Nd or Ce atoms. Interstitial sites near Ce atoms are 3−4 times more populated than the Nd ones, demonstrating that interstitial oxygens tend to form cluster defect with Ce substitutional defects. An effect of this clustering is also observed in the dynamical properties of the Ce-O1 bond.

This work has been partially supported by the Department of Universities and Scientific and Technological Research of the Italian Government (MURST-40%). Dr. Francesco D'Acapito is gratefully acknowledged for help during the XAS data collection and for helpful discussions of the results. The authors are also gratefully indebted to Prof. Calvani for providing the single crystal.

References

1. Y. Tokura, H. Takagi, S. Uchida, Nature **337**, 345 (1989)
2. H. Takagi, S. Uchida, Y. Tokura, Phys. Rev. Lett. **62**, 1197 (1989)
3. M. Scavini, P. Ghigna, G. Spinolo, U. Anselmi Tamburini, G. Chiodelli, G. Flor, A. Lascialfari, S. De Gennaro, Phys. Rev. B **58**, 9385 (1998)
4. A. Lascialfari, P. Ghigna, S. De Gennaro, Int. J. Mod. Phys. B **13**, 1151 (1999)
5. H. Zhang, H. Sato, Phys. Rev. Lett. **70**, 1697 (1993)
6. Y. Onose, Y. Taguchi, K. Ishazaka, Y. Tokura, Phys. Rev. Lett. **87**, 217001 (2001)
7. E.J. Singley, D.N. Basov, K. Kurahashi, T. Uefuji, K. Yamada, Phys. Rev. B **64**, 224503 (2001)
8. H. Oyanagi, Y. Yokoyama, H. Yamaguchi, Y. Kuwahara, T. Katayama, Y. Nishihara, Phys. Rev. B **42**, 10136 (1990)

9. P. Ghigna, G. Spinolo, M. Scavini, U. Anselmi Tamburini, A.V. Chadwick, Physica C **253**, 147 (1995)
10. P. Ghigna, G. Spinolo, A. Filipponi, A.V. Chadwick, P. Hanmer, Physica C **246**, 345 (1995)
11. I. Mangelshots, N.H. Andersen, B. Lebech, A. Wisniewski, C.S. Jacobsen, Physica C **203**, 369 (1992)
12. P.G. Radaelli, J.D. Jorgensen, A.J. Schultz, J.L. Peng, R.L. Greene, Phys. Rev. B **49**, 15322 (1994)
13. A.J. Schultz, J.D. Jorgensen, J.L. Peng, R.L. Greene, Phys. Rev. B **53**, 5157 (1996)
14. G.H. Kwei, S.-W. Cheong, Z. Fisk, F.H. Garzon, J.A. Goldstone, J.D. Thompson, Phys. Rev. B **40**, 9370 (1989)
15. G. Okram Singh, B.D. Padalia, O. Prakash, K. Suba, A.V. Narlikar, L.C. Gupta, Physica C **219**, 156 (1994)
16. G. Spinolo, M. Scavini, P. Ghigna, G. Chiodelli, G. Flor, Physica C **254**, 359 (1995)
17. S.J.L. Billinge, T. Egami, D.R. Richards, D.C. Hinks, B. Dabrowski, J.D. Jorgensen, K.J. Volin, Physica C **179**, 279 (1991)
18. S.J.L. Billinge, T. Egami, Phys. Rev. B **47**, 14386 (1993)
19. X.B. Kan, H. Renevier, J.P. Quintana, J.B. Cohen, Physica C **235-240**, 1279 (1994)
20. X.B. Kan, H. Renevier, J.P. Quintana, J.L. Peng, J.B. Cohen, J. Appl. Phys. **77**, 34 (1995)
21. B.D. Padalia, G. Okram Singh, O. Prakash, S.J. Gurman, J.C. Amiss, J. Phys.: Condens. Matter **9**, 9695 (1997)
22. C.N.R. Rao, J. Mater. Chem. **9**, 1 (1999)
23. P. Ghigna, G. Spinolo, M. Scavini, G. Chiodelli, G. Flor, A.V. Chadwick, Physica C **268**, 150 (1996)
24. J.S. Kim, D.R. Gaskell, Physica C **209**, 381 (1993)
25. W. Sadowski, H. Hagemann, M. Françoise, H. Bill, M. Peter, E. Walker, K. Yvon, Physica C **170**, 103 (1990)
26. A. Filipponi, A.Di Cicco, C.R. Natoli, Phys. Rev. B **52**, 15122 (1995)
27. A. Filipponi, A. Di Cicco, Phys. Rev. B **52**, 15135 (1995)
28. N. Binsted, S.J. Gurman, T.C. Campbell, P.C. Stephenson, EXCURV98 program (Daresbury: SERC Daresbury Laboratory) (1998)
29. *SAINT* and *SADABS*. Bruker AXS Insc., Madison, Wisconsin, USA
30. G.M. Sheldrick, "SHELX-97: a program for structure refinement", University of Gottingen, Gottingen, Germany, 1997
31. R.F. Stewart, M.A. Spackman, "Valray User's Manual", Department of Chemistry, Carnegie-Mellon University, Pittsbourgh, PA, 1983
32. *International Tables for X-ray Crystallography (1974)*, Vol. IV (Birmaingham, Kynoch Press)
33. M. Scavini, Ph.D. thesis, Università di Pavia (1996)
34. D. Haskel, E.A. Stern, F. Dogan, A.R. Moodenbaugh, Phys. Rev. B **61**, 7055 (2000)
35. E. Sevillano, H. Meut, J.J. Rehr, Phys. Rev. B **20**, 4908 (1979)
36. See for example N.L. Saini, A. Lanzara, A. Bianconi, H. Oyanagi, H. Yamaguchi, K. Oka, T. Ito, Physica C **268** 121 (1996); C.Y. Yang, S.M. Heald, J.M. Tranquada, A.R. Moodenbaugh, Youwen Xu, Phys. Rev. B **38**, 6568 (1988)
37. E.F. Paulus, I. Yehia, H. Fuess, J. Rodriguez, T. Vogt, J. Ströbel, M. Klauda, G. Saemann-Ischenko, Solid. State Comm. **73**, 791 (1990)
38. C. Marin, J.Y. Henry, J.X. Boucherle, Solid State Comm. **86**, 425 (1993)
39. I.P. Makarova, V.I. Simonov, M.K. Blomberg, M.J. Merisalo, Acta Cryst. B **52**, 93 (1996)
40. A.N. Petrov, A.Y. Zuev, T.P. Rodionova, J. Am. Ceram. Soc. **82**, 1037 (1999)
41. A. Bram, J. Markl, I.P. Makarova, H. Burzlaff, G. Saemann-Isochenko, V.I. Simonov, Physica C **272**, 209 (1996)
42. F. Sperandini, A.Di Cicco, J. Phys. IV France **7**, C2-1237 (1997); F. Sperandini, A.Di Cicco, M. Gazda, Phys. Rev. B **57**, 6067 (1998)